On the Evolution From Micrometer-Scale Inhomogeneity to Global Overheated Structure During the Intense Joule Heating of a z-Pinch Rod

T. J. Awe, E. P. Yu, K. C. Yates, W. G. Yelton, B. S. Bauer, T. M. Hutchinson, S. Fuelling, and B. B. Mckenzie

Abstract—Ultrafast optical microscopy of metal z-pinch rods pulsed with megaampere current is contributing new data and critical insight into what provides the fundamental seed for the magneto-Rayleigh–Taylor (MRT) instability. A two-frame near infrared/visible intensified-charge-coupled device gated imager with 2-ns temporal resolution and 3-μm spatial resolution captured emissions from the nonuniformly Joule heated surfaces of ultrasmooth aluminum (Al) rods. Nonuniform surface emissions are consistently first observed from discrete, 10-μm scale, subelectronvolt spots. Aluminum 6061 alloy, with micrometer-scale nonmetallic resistive inclusions, forms several times more spots than 99.999% pure Al 5N; 5–10 ns later, azimuthally stretched elliptical spots and distinct strata (40–100 μm wide by 10 μm tall) are observed on Al 6061, but not on Al 5N. Such overheat strata, which are aligned parallel to the magnetic field, are highly effective seeds for MRT instability growth. These data give credence to the hypothesis that early nonuniform Joule heating, such as the electrothermal instability, may provide the dominant seed for MRT.

Index Terms—Electrothermal effects, magnetic fields, optical imaging, plasma pinch, plasma stability.

I. Introduction

IMPLOSION asymmetries generated by the magneto-Rayleigh–Taylor (MRT) instability [1], [2] limit the performance of the magnetically accelerated z-pinch liners (tubes) used to compress high-energy-density plasmas for radiation effects [3], [4], dynamic material properties [5]–[8], and inertial confinement fusion (ICF) studies [9]–[13], but the seed perturbation from which MRT grows is not yet fully understood. Similar to laser-driven ICF, where surface roughness is the dominant seed for the Rayleigh–Taylor instability [14],

azimuthally correlated (lathe-generated) liner-surface roughness was considered the dominant seed for MRT; however, experiments on the Sandia National Laboratories Z Machine show that liners with 10–30 nm initial roughness develop MRT, which is both larger amplitude and more azimuthally correlated than expected [15]–[17]. Alternatively, early in the current pulse, while the metal is at subelectronvolt temperature and well before bulk liner implosion has begun, an azimuthally correlated electrothermal instability (ETI) may grow on the liner's surface to an amplitude of several micrometers [18], [19] (~100 times the initial roughness). ETI is driven by Joule heating and arises from the dependence of electrical resistivity (η) on temperature (T) [20]–[27]. For metals in solid, liquid, and (nonionized) vapor states, with $\partial \eta / \partial T > 0$, hot and cold bands, or azimuthally correlated "strata," can grow, whereas for plasmas ($\partial \eta / \partial T < 0$), axially oriented overheated "filaments" can grow. Simulations demonstrate that after a condensed metal ($\partial \eta / \partial T > 0$) melts and loses strength, temperature and pressure variations drive expansion along strata, providing a relatively large amplitude seed for MRT growth [18], [21], [24], [26], [27]. However, strata formation from a *thick metal*—where the metal is thicker than the magnetic field penetration depth and thus current is carried in a surface skin layer—has until now lacked experimental confirmation.

Which inhomogeneity most virulently drives the early nonuniform Joule heating of the current-carrying surface of a conductor, and whether such nonuniformity can provide the dominant seed for subsequent MRT growth have not yet been experimentally determined. To address such questions requires data on the low-temperature evolution of a metal carrying skin current; the ongoing need for such data motivated this paper.

This manuscript presents unparalleled data on the early nonuniform Joule heating of a thick z-pinch rod. Precision load fabrication (diamond turning and/or electrochemical surface polishing) has been combined with extreme diagnostic resolution to provide data for unique, constraining tests of 3-D magnetohydrodynamic (3-D-MHD) simulations. For Al 6061 alloy, newly observed early phenomena include overheated azimuthally stretched elliptical spots (20–40 μm wide by 10 μm tall) and distinct strata (40–100 μm wide by 10 μm tall). A variety of theoretical and computational studies [18], [21], [24], [26], [27] demonstrate that overheat

strata, which are aligned with the magnetic field, are highly effective seeds of MRT. These data give credence to the hypothesis that early nonuniform Joule heating, including, but not limited to, ETI, may provide the dominant seed for MRT. However, for 99.999% pure Al 5N alloy with little or no inclusions, and meticulous surface preparation, the number of bright spots that initially form on the rod's surface is reduced, and strata formation is eliminated; these data provide a path for potentially mitigating the dominant seed for MRT.

II. EXPERIMENTAL OVERVIEW

Diagnosing the early surface heating of thick metal carrying current in a surface skin layer poses a significant experimental challenge. First, thick metals support 3-D current flow; current will tend to divert around (on the surface) and/or below (deeper than the surface) regions of higher resistivity, which could reduce or even quench local runaway overheating. This may result in more subtle and difficult to diagnose temperature variations than in thin wires or foils [28]–[32]. Next, for ultrasmooth surfaces, nonuniform Joule heating is likely seeded by micrometer -scale variations in the metallic structure (i.e., inclusions, defects, or grain boundaries); diagnostics with micrometer -scale spatial resolution are, therefore, needed to determine if such seeding processes are credible. Furthermore, strata formation is predicted to form in condensed metals ($\partial \eta / \partial T > 0$), which are typically at temperatures below 0.3 eV, and thus weakly radiating in the near infrared (NIR) and visible (VIS). If low-intensity emissions are to be observed, they cannot be overwhelmed by emissions from the nonthermal plasmas common to high-voltage generators (e.g., arcs from load-electrode contacts). Finally, diagnosable striation-form overheated structures may be short lived, growing while $\partial \eta / \partial T > 0$, but then stabilized and/or overwhelmed by much brighter emissions when the surface transitions to the plasma state ($\partial \eta / \partial T < 0$). Thus, diagnostics require a few-nanosecond temporal resolution. In summary, a high spatial (micrometer scale) and temporal (nanosecond scale) resolution intensified gated imager with sensitivity to NIR/VIS emissions is well-suited for examining the nonuniform surface heating of thick metals pulsed with intense current.

Ultrafast microscopy captured emissions from the surface of 1-mm-diameter Al rods [Fig. 1(b)] pulsed to 1 MA in 100 ns by the Zebra pulsed-power driver [33]. Data from such rods emulate the early heating stages of liners imploded on the Z machine, with current flowing in a surface skin layer, megagauss-level surface field, and Joule heating through nonlinear magnetic diffusion. The hardware platform used [Fig. 1(a)] includes compressed metal-to-metal electrical contacts in the load region, and has been shown, through rigorous experimental testing, to consistently mitigate nonthermal plasma formation [34]. A two-frame NIR/VIS intensified-charge-coupled device (ICCD) gated imager with 2-ns temporal resolution and 3-μm spatial resolution had sufficient collection efficiency and gain to record low temperature emissions ($T \geq 0.3$ eV) from Al in the liquid/vapor state yet also had the dynamic range to record emission from ~3-eV plasmas.
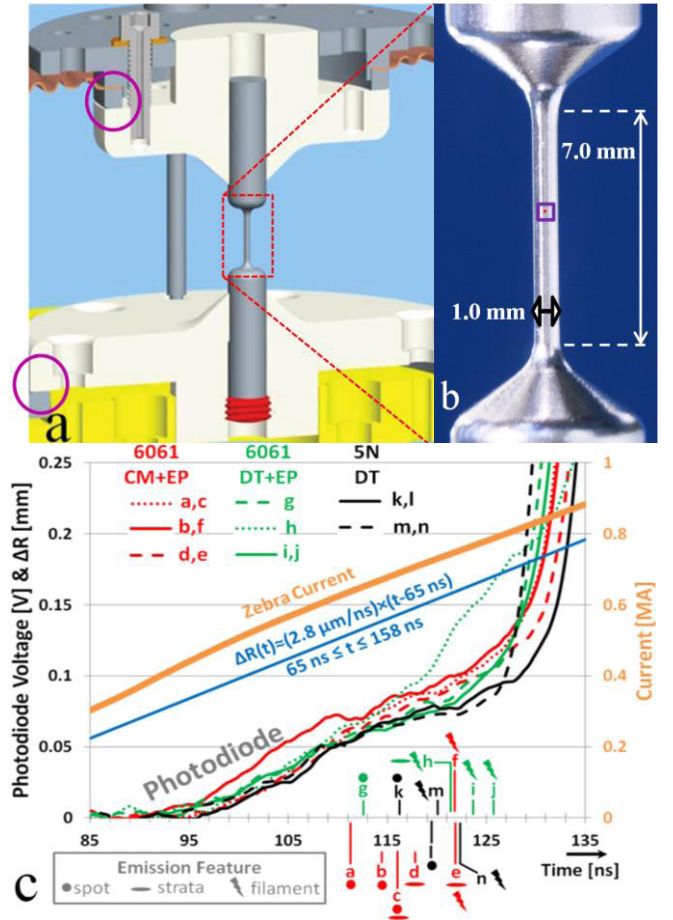

Fig. 1. (a) "Barbell" load mounted in compressed knife-edge anode–cathode coupling hardware. Various features of this hardware (described in detail in [34]) effectively mitigate the nonthermal plasmas that are often produced from electrical connections in high-voltage pulsed power generators. Circles indicate the locations of knife-edge rings used to break through the oxide layers in the Al anode and cathode plates to enable metal-to-metal power-flow connections. (b) Image of a barbell load. The 1-mm-diameter central-rod surface is Joule heated by 2–2.5 MA/cm lineal current density, rising 3.5 kA/cm each nanosecond. Purple box: field of view of the ICCD images in Fig. 3. Red square (inside the purple box): field of view of the scanning electron microscope and WLI images of Fig. 2. (c) Select time-dependent experimental parameters, including a typical Zebra load-current profile [all data are synchronized so that for each shot, $I(t = 100$ ns$) = 500$ kA], and the change in rod radius. Expansion data are quite consistent for the variety of loads discussed in this paper; the data from which the expansion curve was derived are discussed in detail in [35]. Spatially integrated, green-filtered (broadband), self-emission data, recorded using a fast photodiode array, are given for all experiments for which ICCD images are included in Fig. 3. Included along the time axis are labeled tick marks (a–n), which indicate the start time of the intensifier gate pulse for images (a–n) in Fig. 3 [36], as well as the variety of overheat structure observed in each image (spot, strata, filament, or a combination).

III. PRESHOT CHARACTERIZATION OF ALUMINUM SURFACES

Since any perturbation in the resistivity or current density can seed nonuniform Joule heating, load surfaces were characterized using several types of microscopy, prior to experiments. These included scanning electron microscopy [SEM; secondary-electron surface topography, Fig. 2(a), (c), and (e)], energy dispersive spectroscopy (EDS; elemental constituents), and white-light interferometry [WLI; surface topography, Fig. 2(b), (d), and (f)]. Fig. 2(a) and (b) shows an
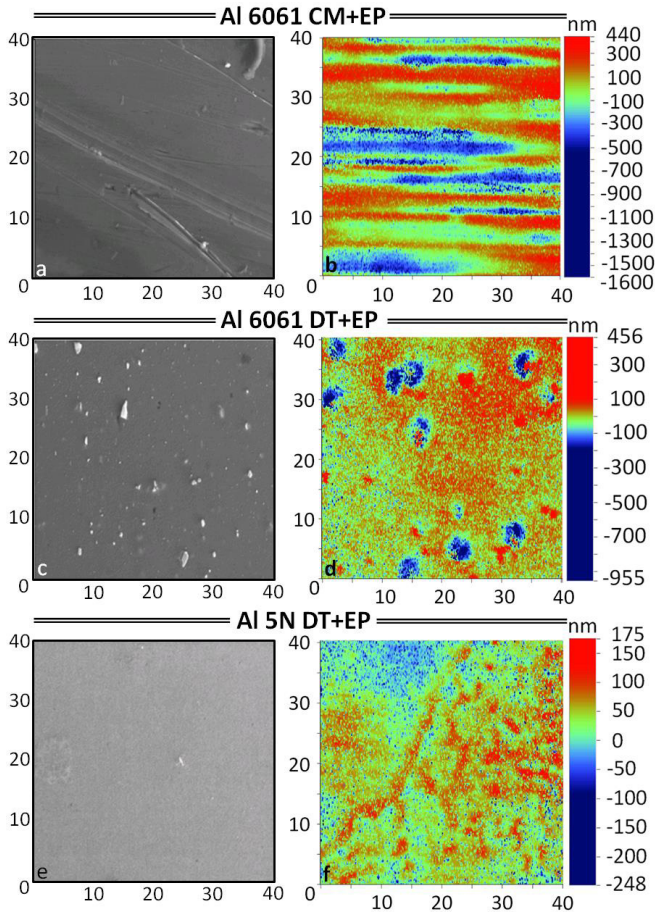
Fig. 2. (a), (c), and (e) SEM (secondary electron) characterization and (b), (d), and (f) WLI characterization of various rod surfaces. Axes are in micrometer. (a) and (b) CM and PO-EP Al 6061 rod. (c) and (d) DT and PO-EP Al 6061 rod. (e) and (f) DT and PO-EP Al 5N rod. The "roughness average" (R_a, the arithmetic average of absolute values of the vertical offset from the mean surface height) calculated for the white-light interferograms in (b), (d), and (f) is 170, 42, and 29 nm, respectively.

Al 6061 rod, which was conventionally machined (CM) and pulse-oxide electrochemically polished (PO-EP) [37]. Power spectrum analysis of SEM and WLI data from such rods indicates a perturbation with 5-μm wavelength is present (due to lathe machining). Fig. 2(c) and (d) shows a single-point-diamond-turned (DT) and PO-EP Al 6061 rod surface. Since DT resulted in submicrometer-amplitude machining perturbations, even minimal Al removal by PO-EP exposes inclusions as the dominant remaining surface defect. EDS indicates that the inclusions are predominantly composed of silicon and magnesium. Finally, Fig. 2(e) and (f) shows an Al 5N (99.999% pure) surface, which was DT and PO-EP. Very few, if any, inclusions are identified, and the surface is nearly perfect, in comparison, although several micrometer-scale defects are still present in Fig. 2(e).

IV. ULTRAFAST MICROSCOPY DATA

A two-frame NIR/VIS ICCD system monitored the evolution of surface emissions from intensely Joule heated Al rods. Emissions from rods of varying alloy and fabrication technique are shown in Fig. 3. In most experiments, two images were captured using separate Andor iStar ICCD cameras [38].

A Questar QM-100 long distance microscope generates an image that is magnified by a 28-mm Nikkor lens and next split using a pellicle membrane. Separate images were focused on the independently gated ICCDs. The system magnification was $M \sim 22$. Approximately, 3-μm spatial resolution was achieved, as determined using an AF-1951 resolution test pattern.

V. ANALYSIS AND DISCUSSION

Certain differences in nonuniform heating can be correlated with the metallic alloy used and/or surface defects specific to the fabrication process. While the earliest observed emissions always originate from discrete spots, the number of spots depends strongly on alloy. Fig. 4 plots the number of spots/mm^2 for 15 images (ten for Al 6061 and five for Al 5N). These data indicate that the number of spots increases with time (current), and at time $\sim$115 ns ($\sim$650 kA), there are 2–9 times more spots/mm^2 for Al 6061 surfaces than for Al 5N surfaces. The dramatic contrast can also be seen by comparing Fig. 3(a)–(c) and (g) with Fig. 3(k) and (l). Also at this time ($\sim$115 ns), the overheated structures on Al 6061 [see Fig. 3(c)–(e) and (h) are dominantly elliptical spots (20–40 μm wide by 10 μm tall] and/or distinct strata (40–100 μm wide by 10 μm tall). By contrast, the Al 5N images show only a hint of these phenomena.

It is interesting to compare the number of spots/mm^2 (Fig. 4) with the number of surface defects/mm^2 in Fig. 2. Evaluating 0.0095 mm^2 of the Al 6061 DT+EP rod surface characterized in Fig. 2(c), there is only one defect with longest dimension $d > 5$ μm (which equates to 100 defects/mm^2, albeit with poor statistics). There are 17 defects (1800 defects/mm^2) with $2.5 < d < 5$ μm, 80 defects (8400 defects/mm^2) with $1 < d < 2.5$ μm, and over 200 000 defects/mm^2 with $d < 1$ μm. This suggests that defects of scale $\sim$5-μm seed the observed spots. While Al 5N rods are essentially inclusion free, a small number of few-micrometer-scale defects do exist on the surface. Such defects possibly seed the relatively small number of spots emitting from Al 5N.

This first-ever observation of azimuthally elongated spots [Fig. 3(c)] and strata [Fig. 3(d), (e), and (h)] in the early heating phase of Al 6061 is significant, as strata are highly effective seed perturbations for the MRT instability. Very few circular spots are seen when elliptical spots and strata are present. Hence, the majority of the latter likely result from azimuthal broadening of initially quasi-spherical resistive imperfections, with subsequent merging of elongated spots into strata. (Simulations show that similar initially isolated ETI-driven perturbations will correlate azimuthally; see [27, Figs. 4 and 5] and relevant discussion.) This would also explain the difference with Al 5N, which did not show strata, because resistive inclusions are far more numerous in Al 6061 than in Al 5N. In addition, some strata could arise from simultaneous brightening of different locations along machining grooves, which were predominantly azimuthal. However, strata are observed not only on Al 6061 CM + EP rods, but also on Al 6061 DT + EP surfaces [Fig. 3(h)] for which machining grooves were mostly
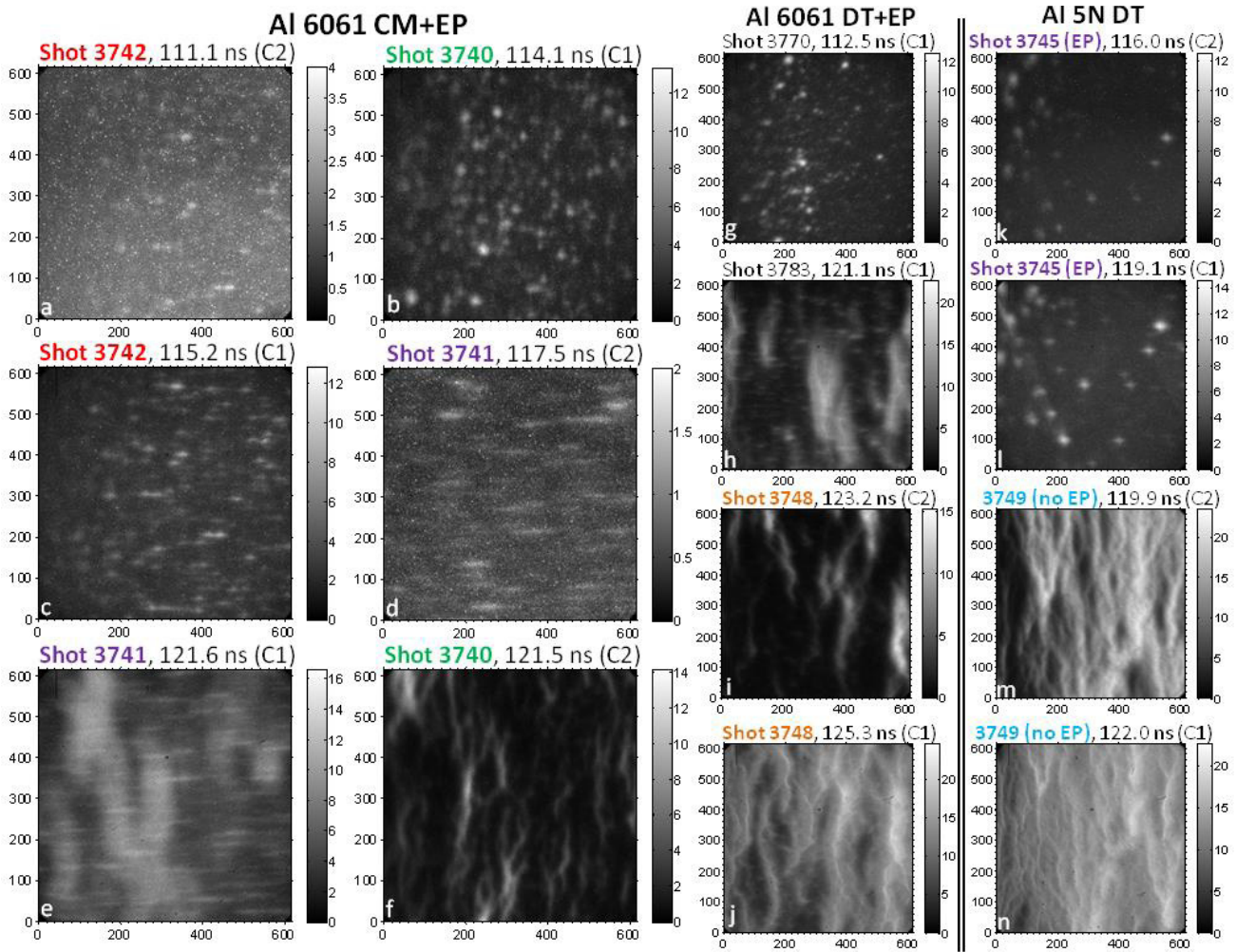
Fig. 3. Images of emissions from the Al rods (a-n). Axes are in micrometer. Color bars are in 1000s of counts per ICCD pixel (Fig. 5 provides a guide for converting from counts to temperature). (a) and (d) have been contrast adjusted to accentuate relatively dim (versus background) overheated features. Doing so also accentuates distributed "hot" pixels which are not due to self-emission from the rod (they are much smaller than image resolution, and also not consistently located in the images from the two cameras); these artifacts are not included when quantifying the number of spots in an image (Fig. 4). There is appreciable overlap in the surface area captured by the two cameras (C1 and C2); in all cases shown, similar surfaces will be 130–140 μm higher in the C1 image. As the current increases, the dominant pattern changes from spots, to strata for Al 6061, to filaments, with a brief overlap between stages [see Fig. 1(c)].

eliminated [see Fig. 2(c) and (d)]. Still, machining might generate unobserved azimuthally oriented variations in Al 6061 through, for example, work hardening, while affecting softer Al 5N differently. Also, given the limited number of Al 5N shots, timing jitter could have led to not capturing images of the brief (~5 ns) phase when strata potentially exist. In summary, we emphasize the significance of the observation of azimuthal strata in the early heating phase—even if great care is taken to minimize surface roughness, strata appear which can then provide the dominant seed for MRT growth.

As surface plasma forms, the observable overheated structures transition to vertically oriented filaments, similar to ETI theory predictions for $\partial \eta / \partial T < 0$. Strata and filaments are observed simultaneously in Fig. 3(e) and (h). In these images, the filaments appear broad and diffuse. Later, for all alloys and surface finishes, bright and sharp vertically oriented plasma filaments form [Fig. 3(f), (i), (j), (m), and (n)].

The histograms in Fig. 5 show that as the emissions from the rod's surface evolve from spots, to strata, to filaments,

they intensify. Histograms in red apply to images dominated by spot emission. For such images, the majority of the rod surface area is relatively cool, and emits weakly, while the high-intensity "foot" of the distribution is due to spot emission. Histograms for images with concurrent strata and filaments (green) are trimodal, with a low intensity contribution due to background below ~5000–6000 counts, a medium intensity contribution due to strata extending to near 8000 counts, and a high intensity contribution due to plasma filaments extending to nearly 15 000 counts. Emissions from plasma filaments are even more intense (black curves), and at higher current, the surface plasma tends to become increasingly uniform (3753).

Experiments capture phenomena, which are clearly 3-D in nature, evolve rapidly over few-nanosecond timescales, and may originate from micrometer-scale features on or within the metal, and therefore modeling the pertinent physics requires a 3-D and highly resolved simulation. Preliminary results using the 3-D-MHD code ALEGRA [39] inform how global structures (e.g., strata or filaments) can evolve from isolated
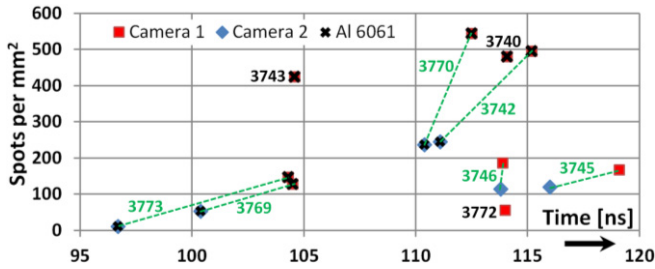
Fig. 4. Number of spots/mm² for select ICCD images. Red squares (blue diamonds) indicate data from camera 1 (camera 2). Al 6061 data are overlaid with a black "x" (others are Al 5N data). Green lines connect data points from a single shot. Images from camera 1 contain more discernable spots than those from camera 2. This is likely mostly due to two effects. First, camera 1 images (for a given shot) were typically gathered 2–4 ns later than those for camera 2, and the number of spots increases with time. Second, the two cameras had appreciably different spectral responses. For example, camera 1 was ∼6 times more sensitive than camera 2 at 500 nm, while camera 2 was more sensitive in the NIR. Thus, camera 1 was more sensitive to the higher temperature spots, and less sensitive to the cooler background, resulting in higher contrast.
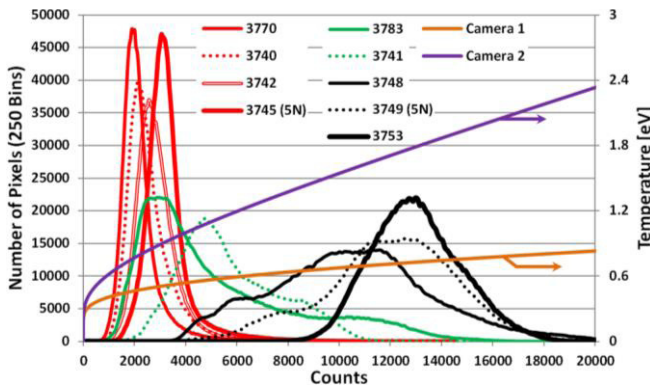

Fig. 5. Histograms generated for certain camera 1 images. Red, green, and black curves present data for images dominated by spot, strata plus filament, and filament emission, respectively. Also, included in the plot are curves that provide a guide for converting from ICCD counts to a lower-bound temperature [eV] (using the secondary vertical axis) for camera 1 (orange) and camera 2 (purple). The conversions assume both blackbody emission and a surface emissivity of 1 and consider the best available data on imaging system setup and parameters (i.e., emitter area, solid angle, filter transmission, glass transmission, and intensifier quantum efficiency). In general, the camera 1 conversion suggests slightly lower temperatures than the camera 2 conversion for similar emission features; this issue has not yet been resolved, and may require detailed characterization rather than reliance on manufacturer datasheets.

surface defects. For example, our ongoing simulations using a 0.5-μm Eulerian mesh, tabular SESAME equation of state, and Lee–More–Desjarlais electrical and thermal conductivities [40] show that the 3-μm radius hemispherical pits or resistive inclusions will indeed seed spot formation. Spots then elongate in the direction perpendicular to the current flow; this occurs because current bends azimuthally around the defect, leading to enhanced current density at the edges, which results in overheating and increased local resistivity. Through this process, closely neighboring defects will stretch and eventually connect azimuthally to form elongated strata (in qualitative agreement with the results in [27]); such strata readily couple to the MRT instability. Simulations show that the material surrounding the defect soon explodes and generates an expanding plasma plume (these 3-D ALEGRA simulations show that strata remain and grow below the plasma surface). Competition between cooling due to expansion and

Joule heating in the plasma plume leads to preferential growth in the axial direction, eventually resembling the filaments observed experimentally. (Plasma filament formation was not considered in [21] and [27].) A full discussion of 3-D simulations will be the topic of a future publication [41].

ACKNOWLEDGMENT

REFERENCES

[1] E. G. Harris, "Rayleigh–Taylor instabilities of a collapsing cylindrical shell in a magnetic field," *Phys. Fluids*, vol. 5, no. 9, pp. 1057–1062, 1962.

[2] Y. Y. Lau, J. C. Zier, I. M. Rittersdorf, M. R. Weis, and R. M. Gilgenbach, "Anisotropy and feedthrough in magneto-Rayleigh–Taylor instability," *Phys. Rev. E, Stat. Phys. Plasmas Fluids Relat.*, vol. 83, p. 066405, Jun. 2011.

[3] J. E. Bailey *et al.*, "Dynamic hohlraum radiation hydrodynamics," *Phys. Plasmas*, vol. 13, no. 5, p. 056301, 2006.

[4] G. A. Rochau, "High performance capsule implosions driven by the Z-pinch dynamic hohlraum," *Plasma Phys. Control. Fusion*, vol. 49, no. 12B, pp. B591–B600, 2007.

[5] M. D. Knudson, D. L. Hanson, J. E. Bailey, C. A. Hall, J. R. Asay, and C. Deeney, "Principal Hugoniot, reverberating wave, and mechanical reshock measurements of liquid deuterium to 400 GPa using plate impact techniques," *Phys. Rev. B, Condens. Matter*, vol. 69, pp. 144209–144220, Apr. 2004.

[6] R. E. Reinovsky, "Instability growth in magnetically imploded high-conductivity cylindrical liners with material strength," *IEEE Trans. Plasma Sci.*, vol. 30, no. 5, pp. 1764–1776, Oct. 2002.

[7] J. E. Bailey *et al.*, "A higher-than-predicted measurement of iron opacity at solar interior temperatures," *Nature*, vol. 517, pp. 56–59, Jan. 2015.

[8] M. R. Martin *et al.*, "Solid liner implosions on Z for producing multi-megabar, shockless compressions," *Phys. Plasmas*, vol. 19, no. 5, p. 056310, 2012.

[9] S. A. Slutz *et al.*, "Pulsed-power-driven cylindrical liner implosions of laser preheated fuel magnetized with an axial field," *Phys. Plasmas*, vol. 17, no. 5, p. 056303, 2010.

[10] S. A. Slutz and R. A. Vesey, "High-gain magnetized inertial fusion," *Phys. Rev. Lett.*, vol. 108, p. 025003, Jan. 2012.

[11] M. E. Cuneo *et al.*, "Magnetically driven implosions for inertial confinement fusion at Sandia National Laboratories," *IEEE Trans. Plasma Sci.*, vol. 40, no. 12, pp. 3222–3245, Dec. 2012.

[12] A. B. Sefkow *et al.*, "Design of magnetized liner inertial fusion experiments using the Z facility," *Phys. Plasmas*, vol. 21, no. 7, p. 072711, 2014.

[13] M. R. Gomez *et al.*, "Experimental demonstration of fusion-relevant conditions in magnetized liner inertial fusion," *Phys. Rev. Lett.*, vol. 113, p. 155003, Oct. 2014.

[14] S. W. Haan *et al.*, "Point design targets, specifications, and requirements for the 2010 ignition campaign on the National Ignition Facility," *Phys. Plasmas*, vol. 18, no. 5, p. 051001, 2011.

[15] D. B. Sinars *et al.*, "Measurements of magneto-Rayleigh–Taylor instability growth during the implosion of initially solid metal liners," *Phys. Plasmas*, vol. 18, no. 5, p. 056301, 2011.

[16] R. D. McBride *et al.*, "Penetrating radiography of imploding and stagnating beryllium liners on the Z accelerator," *Phys. Rev. Lett.*, vol. 109, p. 135004, Sep. 2012.

[17] R. D. McBride *et al.*, "Beryllium liner implosion experiments on the Z accelerator in preparation for magnetized liner inertial fusion," *Phys. Plasmas*, vol. 20, no. 5, p. 056309, 2013.

[18] K. J. Peterson *et al.*, "Electrothermal instability mitigation by using thick dielectric coatings on magnetically imploded conductors," *Phys. Rev. Lett.*, vol. 112, p. 135002, Apr. 2014.

[19] T. J. Awe *et al.*, "Experimental demonstration of the stabilizing effect of dielectric coatings on magnetically accelerated imploding metallic liners," *Phys. Rev. Lett.*, vol. 116, no. 6, p. 065001, 2016.

[20] D. D. Ryutov, M. S. Derzon, and M. K. Matzen, "The physics of fast Z pinches," *Rev. Mod. Phys.*, vol. 72, pp. 167–223, Jan. 2000.

[21] K. J. Peterson *et al.*, "Electrothermal instability growth in magnetically driven pulsed power liners," *Phys. Plasmas*, vol. 19, no. 9, p. 092701, 2012.

[22] V. I. Oreshkin *et al.*, "Wire explosion in vacuum: Simulation of a striation appearance," *Phys. Plasmas*, vol. 11, no. 10, p. 4771, 2004.

[23] V. I. Oreshkin, "Overheat instabilities in the electric explosion of wires," *Tech. Phys. Lett.*, vol. 35, no. 1, pp. 36–39, Jan. 2009.

[24] V. I. Oreshkin, "Thermal instability during an electrical wire explosion," *Phys. Plasmas*, vol. 15, no. 9, p. 092103, 2008.

[25] A. G. Rousskikh *et al.*, "Study of the strata formation during the explosion of a wire in vacuum," *Phys. Plasmas*, vol. 15, no. 10, p. 102706, 2008.

[26] K. J. Peterson *et al.*, "Simulations of electrothermal instability growth in solid aluminum rods," *Phys. Plasmas*, vol. 20, no. 5, p. 056305, 2013.

[27] J. D. Pecover and J. P. Chittenden, "Instability growth for magnetized liner inertial fusion seeded by electro-thermal, electro-choric, and material strength effects," *Phys. Plasmas*, vol. 22, no. 10, p. 102701, 2015.

[28] G. S. Sarkisov, K. W. Struve, and D. H. McDaniel, "Effect of current rate on energy deposition into exploding metal wires in vacuum," *Phys. Plasmas*, vol. 11, no. 10, pp. 4573–4581, 2004.

[29] D. B. Sinars *et al.*, "The effect of insulating coatings on exploding wire plasma formation," *Phys. Plasmas*, vol. 7, no. 2, pp. 429–432, 2000.

[30] V. I. Oreshkin, K. V. Khishchenko, P. R. Levashov, A. G. Rousskikh, and S. A. Chaikovskii, "Strata formation at fast electrical explosion of cylindrical conductors," *High Temperature*, vol. 50, no. 5, pp. 584–595, Sep. 2012.

[31] R. B. Baksht, A. G. Rousskikh, A. S. Zhigalin, V. I. Oreshkin, and A. P. Artyomov, "Stratification in Al and Cu foils exploded in vacuum," *Phys. Plasmas*, vol. 22, no. 10, p. 103521, 2015.

[32] L. Atoyan *et al.*, "Helical plasma striations in liners in the presence of an external axial magnetic field," *Phys. Plasmas*, vol. 23, no. 2, p. 022708, 2016.

[33] B. S. Bauer *et al.*, "The Dense Z-Pinch Program at the University of Nevada, Reno," in *Proc. 4th Int. Conf. Dense Z-Pinches*, vol. 409. Vancouver, BC, Canada, 1997, p. 153.

[34] T. J. Awe, B. S. Bauer, S. Fuelling, and R. E. Siemon, "Mitigation of nonthermal plasma production to measure the pulsed magnetic field threshold for the thermal formation of plasma from thick aluminum surfaces," *Phys. Plasmas*, vol. 18, no. 5, p. 056304, 2011.

[35] T. J. Awe, B. S. Bauer, S. Fuelling, I. R. Lindemuth, and R. E. Siemon, "Experimental investigation of thermal plasma formation from thick aluminum surfaces by pulsed multimegagauss magnetic field," *Phys. Plasmas*, vol. 17, no. 10, p. 102507, 2010.

[36] *Image Timing Has a ±3 ns Uncertainty, Which is Mostly Due to Electrical-to-Optical and Optical-to-Electrical Converters That Were Included Both in the Camera's Trigger Line and in the Camera's Intensifier Output Monitor Line.*

[37] *Pulse Anodized to Selectively Form Layers of Oxides at Machining Groove Peaks, and Then Selectively Etching Away the Oxides.*

[38] *Camera 1 (C1) Was Model DH734-18F-A3, While Camera 2 (C2) Was Model DH334T-18U-73.*

[39] A. C. Robinson *et al.*, "ALEGRA: An arbitrary Lagrangian–Eulerian multimaterial, multiphysics code," in *Proc. 46th AIAA Aerosp. Sci. Meeting Exhibit*, Reno, NV, USA, Jan. 2008, pp. 1–39, paper AIAA-2008-1235. [Online]. Available: http://arc.aiaa.org/doi/abs/10.2514/6.2008-1235

[40] M. P. Desjarlais, J. D. Kress, and L. A. Collins, "Electrical conductivity for warm, dense aluminum plasmas and liquids," *Phys. Rev. E, Stat. Phys. Plasmas Fluids Relat.*, vol. 66, p. 025401(R), Aug. 2002.

[41] E. P. Yu, Sandia Nat. Lab., Albuquerque, NM, USA.